Raman spectroscopy and TEM characterization of solid particulate matter emitted from soot generators and aircraft turbine engines

Saffaripour, Meghdad; Tay, Li-Lin; Thomson, Kevin A.; Brem, B. T.; Durdina, Lukas; Johnson, Mark; Smallwood, Greg J.

Publisher's version / Version de l'éditeur:
https://doi.org/10.1080/02786826.2016.1274368
Aerosol Science and Technology, 2016-12-23

AEROSOL SCIENCE AND TECHNOLOGY
http://dx.doi.org/10.1080/02786826.2016.1274368

Raman spectroscopy and TEM characterization of solid particulate matter emitted from soot generators and aircraft turbine engines

Meghdad Saffaripour[a], Li-Lin Tay[a], Kevin A. Thomson[a], Gregory J. Smallwood[a], Benjamin T. Brem[b], Lukas Durdina[b], and Mark Johnson[c]

[a]National Research Council Canada, Ottawa, Ontario, Canada; [b]EMPA, Swiss Federal Laboratories for Materials Science and Technology, Dübendorf, Switzerland; [c]Rolls–Royce, plc., Derby, England, United Kingdom

ABSTRACT

To obtain reliable mass concentrations of solid particulate matter (PM) in the exhaust emissions from engines using optical instruments, it is essential that the solid PM used for instrument calibration has similar optical properties to the solid PM emitted from the engines being tested. The solid PM emitted from combustion engines is predominantly soot. The optical properties of soot are dictated by its chemical structure, size, and morphology. In this work, the chemical bond structure, primary-particle diameters, aggregate sizes, and morphological parameters of the soot emitted from two laboratory soot generators, widely used for calibrating instruments, are compared to those of soot emitted from three aircraft turbine engines using Raman spectroscopy and transmission electron microscopy. The Raman spectral properties, size, and morphology of soot emitted from aircraft engines are distinctly different from the properties of soot emitted from the soot generators operating under globally near-stoichiometric and fuel-rich conditions. These differences can be attributed to the variations in the size and orientation of the graphitic crystallites, amorphous-carbon content, amount of polyacetylene compounds, deposition of organic material, and extent of oxidation. Conversely, general agreement is observed between the chemical structure, size, and morphology of soot emitted from aircraft engines and the soot emitted from the soot generators operating at globally fuel-lean conditions. The findings of this investigation can be useful for identifying suitable soot particles for the calibration of instruments to measure the mass concentration of solid PM emissions from engines, and for other types of soot.

ARTICLE HISTORY
Received 7 September 2016
Accepted 14 December 2016

EDITOR
Matti Maricq

1. Introduction

The concern over the solid particulate matter (PM) emissions of commercial aircraft is growing because of their adverse impacts on human health and climate. These emissions, which typically peak during the takeoff and climb-out operating modes, increase the risk of respiratory and cardiovascular diseases among the communities living near airports (Boyle 1996; Pope III 2000; Donaldson et al. 2001; Hudda et al. 2014; MDPH 2014). Aircraft-generated solid particulate matter is predominantly soot, and is also predominantly black carbon, as there are only minor differences in the solid phase of aircraft-generated particulate matter, soot, and black carbon. Black carbon alters the Earth's radiation budget directly by absorbing and scattering the incoming solar radiation (Bond et al. 2013). In addition, by acting as vapor condensation nuclei, these particles initiate contrails and affect the radiative properties of clouds (Denman and Brasseur 2007; Forster and Ramaswamy 2007). To better understand and assess these unfavorable impacts, accurate quantitative measurement of soot emissions from aircraft turbine engines is crucial.

Various optical instruments have been developed in recent years to measure the mass concentration of emitted soot. Generally, mass concentration is quantified by an empirical correlation factor obtained from the calibration of each instrument. Typically, the correlation factor is determined by comparing the optical response of the instrument to a reference source of soot particles. The soot particles used for calibrating instruments are commonly produced by soot generators or laboratory flames. However, the performance of the mass-concentration instruments can be highly sensitive to the optical properties of the particles (Sharma et al. 2002; Slowik et al. 2007; Baumgardner et al. 2012). Therefore, it is crucial that the

CONTACT Meghdad Saffaripour msaffaripour@gmail.com National Research Council Canada, Black-Carbon Metrology, Building M-9, 1200 Montreal Road, Ottawa, ON K1A 0R6, Canada.

Color versions of one or more of the figures in this article can be found online at www.tandfonline.com/uast.

Supplemental data for this article can be accessed on the publisher's website.

particles used for instrument calibration have similar optical properties as those emitted from the test engines. It has been shown that the correlation factors for the optical instruments depend strongly on the source, type, and composition of soot particles (Liousse et al. 1993; Sharma et al. 2002). Hence, soot particles emitted from soot generators and aircraft turbine engines might have significantly different optical properties, depending on the combustion conditions under which the soot particles nucleate and grow (Vander Wal and Tomasek 2004; Vander Shaddix et al. 2005; Wal 2005; Raj et al. 2010).

The optical properties of soot particles depend strongly on their chemical bond structure (Rosen et al. 1978; Mertes et al. 2004; Shaddix et al. 2005) as well as their size and morphology (Faeth and Köylü 1995; Colbeck et al. 1997; Liu and Mishchenko 2005; Adachi et al. 2007). Therefore, having knowledge of these characteristics is necessary for comparing the optical properties of soot particles. Raman spectroscopy, which is extremely sensitive to chemical bonds and vibrational frequencies of molecules, is an ideal method to obtain information about the chemical structure of particle samples. Analysis of the transmission electron microscope (TEM) images of particles is a well-established method to measure the physical size of both primary particles and soot aggregates, and to provide information about the fractal-like aggregated morphology of particles (Dobbins and Megaridis 1987; Köylü et al. 1995).

In the present work, the Raman spectral parameters, the size of primary soot particles and aggregates, and the morphological parameters of soot emitted from two soot generators, widely used as sources for calibrating mass-concentration instruments, and the solid PM emitted from three different aircraft turbine engines are measured. To accomplish that, Raman spectroscopy and TEM characterizations are conducted. The objective of this study is to evaluate and compare the chemical structure and morphology of soot emitted from aircraft turbine engines and soot generators. This information will be useful to identify suitable soot particle sources for the calibration of soot mass-concentration instruments for the purpose of measuring the mass concentration of solid PM emissions from engines. Further, it may also be useful for identifying suitable soot particles to be used when calibrating instruments to measure other types of soot, such as from biogenic sources or ambient black carbon.

2. Methods

2.1. Soot generators

The Miniature Combustion Aerosol Standard (MiniCAST), from Jing Ltd., is a commercial soot generator commonly used for research and instrument-calibration purposes (Giechaskiel et al. 2010; Gysel et al. 2012; Mamakos et al. 2013; Maricq 2014; Moore et al. 2014). In the present work, a MiniCAST Model 5201 Type C has been used, which generates soot with a laminar propane/air coflow diffusion flame quenched by a nitrogen jet. The particle stream is diluted with compressed air. By adjusting the flow rates of fuel, fuel diluent (N_2), combustion air, dilution air, and quench gas (N_2), flames with different global fuel-air equivalence ratios (φ), which are quenched at different relative heights, are obtained, which emit particles with various chemical and physical properties. In addition to the MiniCAST, an inverted coflow methane/air diffusion flame, which is another widely used soot generator for instrument calibration and research (Stipe et al. 2005; Coderre et al. 2011; Ghazi et al. 2013), has been used in the present work. The inverted design prevents flame instabilities caused by buoyancy-induced flow acceleration. Both soot generators provide a stable source of particles with minimal hour-to-hour and day-to-day fluctuations.

The chemical and physical properties of the soot emitted from the soot generators are characterized over a wide range of flame conditions, categorized into 14 setpoints. The flow rates of the fuel and oxidation air have been varied to generate flames with global equivalence ratios (φ) ranging from 0.74 to 1.33. φ is defined as

$$\varphi = \frac{(m_{fuel}/m_{ox.air})_{actual}}{(m_{fuel}/m_{ox.air})_{stoichiometric}} \quad [1]$$

in which m_{fuel} is the mass flow rate of the fuel and $m_{ox.air}$ is the mass flow rate of the oxidation air. Note that this is a non-premixed flame. The global equivalence ratio represents the total flows of fuel and oxidation air, and does not imply that there is complete mixing; therefore, not all of the oxidation air participates in the combustion reactions.

The first group of MiniCAST setpoints used had a fixed fuel flow rate of 60 mL/min and the flame global equivalence ratios were between 0.94 and 1.33, i.e., globally near-stoichiometric and fuel-rich conditions. These setpoints are referred to as the fuel-rich (FR) setpoints. The second group of MiniCAST setpoints had varying fuel flow rates and flame global equivalence ratios between 0.74 and 0.86, i.e., globally fuel-lean conditions. These setpoints are referred to as the fuel-lean (FL) setpoints. The inverted diffusion flame has been tested only at one setpoint, with a globally fuel-lean condition ($\varphi =$ 0.79). Three of the FR setpoints, i.e., setpoints FR3, FR4, and FR5, include nitrogen dilution of the fuel stream (an option with the MiniCAST devices) to examine its effect on soot properties. Table 1 presents the flame properties

Table 1. Properties of the flames used in the soot generators at 14 different setpoints. These properties include the soot generator type, fuel, flow rates, and global equivalence ratio (φ). (Inverted = Inverted coflow diffusion flame).

			Flow rates					
Setpoint	Soot generator	Fuel	Fuel (mL/min)	Fuel dilution N_2 (mL/min)	Oxidation air (L/min)	Dilution air (L/min)	Quench N_2 (L/min)	φ
FR1	MiniCAST	C_3H_3	60	0	1.1	20	7	1.33
FR2	MiniCAST	C_3H_3	60	0	1.3	20	7	1.12
FR3	MiniCAST	C_3H_3	60	200	1.5	10	7	0.97
FR4	MiniCAST	C_3H_3	60	250	1.5	10	7	0.97
FR5	MiniCAST	C_3H_3	60	280	1.5	10	7	0.97
FR6	MiniCAST	C_3H_3	60	0	1.55	20	7	0.94
FL1	MiniCAST	C_3H_3	55	0	1.55	20	7	0.86
FL2	MiniCAST	C_3H_3	55	0	1.6	20	7	0.84
FL3	MiniCAST	C_3H_3	60	0	1.75	20	7	0.83
FL4	MiniCAST	C_3H_3	52	0	1.6	20	7	0.79
FL5	Inverted	CH_4	1370	0	16.6	50	N/A	0.79
FL6	MiniCAST	C_3H_3	55	0	1.7	20	7	0.79
FL7	MiniCAST	C_3H_3	50	0	1.6	20	7	0.76
FL8	MiniCAST	C_3H_3	55	0	1.8	20	7	0.74

at all the setpoints for the soot generators used in this study.

In many instances, the output of the soot generator has mass concentrations of soot that are higher than those necessary for calibration. To deal with this, secondary dilution of the soot stream is performed. To assess the impact of changing the dilution ratio on the results, multiple samples have been collected and analyzed at some of the setpoints while varying the secondary dilution levels.

2.2. Aircraft turbine engines

The soot emitted from three aircraft turbine engines is studied, two turboshaft engines based on a late-1950s design and a more modern in-production turbofan engine. All three engines use standard Jet A-1 fuel as the energy source. By varying the speeds and loads of the turboshaft engines and varying the thrust and speed levels of the turbofan engine, particles with different characteristics are emitted, representing a range of in-service operating conditions. Table 2 shows the operating modes of the engines and the estimated global equivalence ratios for these ranges of conditions. The turbine engines are equipped with rich-burn, quick-mix, lean-burn (RQL) combustors; therefore, the fuel-air equivalence ratios vary throughout the combustor. In the present work, the global equivalence ratio, φ, for the whole combustor is estimated based on the overall air-to-fuel ratio calculated using measured CO_2 concentrations at the exit plane of the turbine. This is a reasonable approach because gas temperatures at the combustor exit can be as high as 2000 K, showing that combustion and the soot formation and oxidation processes continue throughout the combustor. To estimate φ, a stoichiometric air-to-fuel ratio of 14.7, based on a Jet A-1 surrogate (Saffaripour et al. 2011), is used. For the turbofan engine, φ varies between ~0.13 and ~0.29, increasing with engine's thrust and speed. However, for the turboshaft engines, φ varies between ~0.15 and ~0.25, decreasing as the engine speed is increased. Multiple samples have been collected from the turbine exhaust and treated with different dilution levels to assess the reproducibility of the results.

2.3. Sampling methods

Samples from the aircraft gas turbine exhaust are acquired with the sampling system documented in SAE AIR6241 (2013). Samples from the soot generators are acquired after transport through lines following the principles of SAE AIR6241 (conductive 3/8″ I.D. tubing, 1 μm cut-point cyclone, narrow angle flow splitters) and dilution.

A point-to-plane electrostatic precipitator, ESPnano from DASH Connector Technology, is used for collecting

Table 2. The properties of the engine setpoints used in the present study, including the engine type, engine speed, thrust level or shaft horse power (shp), and the estimated global equivalence ratio, φ. The high-pressure turbine speed is provided for the turboshaft engines and the fan speed is provided for the turbofan engine.

Setpoint	Engine type	Speed (rpm)	Thrust (% of full)	Load (shp)	φ
E1-1	Turboshaft 1	13,000	—	70	0.25
E1-2	Turboshaft 1	21,000	—	630	0.18
E1-3	Turboshaft 1	22,000	—	770	0.17
E1-4	Turboshaft 1	23,000	—	950	0.16
E1-5	Turboshaft 1	24,000	—	1150	0.15
E2-1	Turboshaft 2	13,000	—	70	0.25
E2-2	Turboshaft 2	22,000	—	770	0.17
E2-3	Turboshaft 2	23,000	—	950	0.16
E3-1	Turbofan	1000	3	—	0.13
E3-2	Turbofan	4200	65	—	0.25
E3-3	Turbofan	4700	85	—	0.29

particle samples. In this device, a high-voltage electric field (~5 kV), created using a sharp needle as the anode and a flat surface as the cathode, charges the particles during the corona discharge (Miller et al. 2010). The electric field drives the particles toward a grounded platform onto which the sampling substrate has been attached.

For Raman-spectroscopy studies, samples are collected on Substratek grids, from Ted Pella, with a gold coating on a 3-mm diameter gold mesh. For these grids, the surface is smooth, and Raman spectra of a region covered with soot are acquired. Alternatively, some of the samples have been collected on preheated quartz filters using unheated filter holders and without the use of the electrostatic precipitator. For these filters, the surface is rough, necessitating that Raman spectra of individual particles be measured. It has been confirmed that there is a good agreement between the results using these two sampling approaches. In total, 10 samples have been collected for the FR setpoints, 12 samples for the FL setpoints, and 27 samples for the aircraft turbine engines.

For TEM imaging, particle samples are collected on carbon-coated copper TEM grids, also from Ted Pella. TEM samples are collected for the following soot-generator setpoints: FR1, FR2, FR6, FL2, FL3, FL7, and FL8. The turbine engine samples are collected from the exhaust of turboshaft engine 1 at the E1-1, E1-2, and E1-3 setpoints. Multiple samples are collected at some MiniCAST and engine setpoints to confirm the repeatability of results.

2.4. Raman spectroscopy measurements

The Raman spectra have been acquired with a commercial microRaman system (LabRAM HR, Horiba Jobin Yvon). Soot samples are excited by 632.8 nm radiation at a power of 0.17 mW to avoid excessive sample heating. Incident radiation is coupled into an Olympus BX51 optical microscope and focused to a 1.6 μm diameter spot through a Leica 50× low-working-distance objective with a numerical aperture of 0.55. The same objective also collects the retro-reflected radiation and guides it through a notch filter that removes the Rayleigh-scattered radiation. All Raman spectra have been collected with a 20 s integration period and are averaged over six scans. The Raman signal is recorded over a frequency range of 646–2792 cm^{-1} with a resolution of 2 cm^{-1}. For samples that are deposited on gold TEM grids, a large number of Raman spectra (up to a few thousand) are acquired and a selected number of them are averaged. For samples collected on the quartz filters, the Raman spectra of five different particles are averaged to obtain the mean value. Spectroscopy and optical-imaging tests have been conducted to make sure that laser irradiation at the selected power does not cause any change to the Raman signature of soot samples. To rule out excitation energy-dependent Raman effects, two of the samples were studied using 785 nm excitation radiation with the incident power of 0.12 mW focused through the same objective. A brief description of Raman spectroscopy is provided in Section 1 of the online supplementary information (SI).

The Raman spectrum of typical soot is composed of two broad and overlapping peaks, as shown in Figure S2 (a) of the SI. The ideal crystalline graphitic structure in soot, which consists of sp^2-bonded carbon atoms in unreactive basal planes, gives rise to the G band (graphite band) centered at a frequency of about 1591 cm^{-1} (Dresselhaus and Dresselhaus 1982). However, most graphitic materials, including soot, have different types of defects in their graphitic structure (Pimenta et al. 2007). Strong defects generally occur at the edge planes of the graphitic crystallites, which induce the D band (defect band) centered at about 1344 cm^{-1}. More detailed investigations of the Raman spectra of carbonaceous material have shown that these spectra can be better represented with a fit of five different bands (Cuesta et al. 1994; Sadezky et al. 2005), shown in Figure S2b. The physical origins of these five bands are presented briefly in Table 3 and with more details in Section 2 of the SI.

Table 3. The spectroscopic origins of the bands that constitute the Raman spectra of soot, in order of increasing Raman shift (more details are provided in Section 2 of the SI).

Band	Center	Origin
D_4	1200 cm^{-1}	Carbon atoms with sp^3 and intermediate sp^2-sp^3 hybridization states (Bacsa et al. 1993), the latter one possibly caused by curved PAH layers in graphitic crystallites (Jäger et al. 1999), and single carbon-carbon bonds in polyacetylene-like compounds (Shirakawa et al. 1973; Harada et al. 1980; Fitchen 1982; Ishida et al. 1986; Lopez-Rios et al. 1996)
D_1	1350 cm^{-1}	Defects occurring at the edge planes of the graphitic crystallites (Pimenta et al. 2007; Dresselhaus and Dresselhaus 1982)
D_3	1500 cm^{-1}	The amorphous-carbon compounds, which are complex mixtures of sp^2- and sp^3-bonded carbon atoms with no order, and impurity ions, such as fluoride, calcium, and potassium (Cuesta et al. 1994; Jawhari et al. 1995; Sadezky et al. 2005), as well as the internal vibrational modes in small graphitic domains related to the asymmetric breathing of the carbon rings and the C–C stretching of internal and edge carbons (Parent et al. 2016)
G	1580 cm^{-1}	Ideal crystalline graphitic structure that consists of sp^2-bonded carbon atoms in unreactive basal planes (Dresselhaus and Dresselhaus 1982)
D_2	1620 cm^{-1}	The structural disorder associated with the PAH layers at the boundaries of the crystallites, i.e., those that are not sandwiched between other PAH layers, (Dresselhaus and Dresselhaus 1982; Sze et al. 2001)

Table 4. The center and FWHM of the bands along with their standard deviations, averaged over all the 49 samples under study.

Band	Band-center mean (cm^{-1})	Std. of center (% of mean)	B-FWHM mean (cm^{-1})	Std. of FWHM (% of mean)
D_4	1190	2.5	166	14.8
D_1	1343	0.5	165	11.9
D_3	1536	1.0	165	10.9
G	1591	0.4	51	17.5
D_2	1618	0.3	43	14.2

Quantifying the five bands present in the Raman spectra of soot provides a wealth of information about the chemical structure of soot and enables the comparisons of different soot materials. In the present work, the Raman spectral analysis approach of Sadezky et al. (2005) has been followed. Lorentzian band shapes have been used for the G, D_1, D_2, and D_4 bands, and a Gaussian band shape has been selected to model the D_3 band (Cuesta et al. 1994; Jawhari et al. 1995; Sadezky et al. 2005). More details about the spectral analysis and the curve fitting procedure are provided in Section 3 of the SI.

Table 4 shows the mean values of the center and full width at half maximum (FWHM) of the bands used to model the measured Raman spectra along with their standard deviations. The presented values are averaged over all the 49 samples studied in the present work. The standard deviations of the band centers are within 0.3–2.5% of the mean values, showing that the sample-to-sample variations of the band positions are negligible. The standard deviations of the band widths (FWHM) show a larger variation between the samples, within 10.9–17.5% of the mean values.

2.5. Transmission electron microscope measurements

The particulate samples are imaged using a Philips CM20 TEM, operating at an accelerating voltage of 120 kV and under high-vacuum condition. Projected, i.e., two-dimensional, TEM images of soot aggregates are captured using a Gatan CCD camera, with 1024×1024 pixel dimensions. To find the relationship between the projected properties of aggregates and their actual, i.e., three-dimensional, morphology, Köylü et al. (1995) studied the projected images of aggregates captured from different angles. The data analysis approach used in the present work, which is based on the findings of Köylü et al. (1995), is capable of recovering the actual soot size and morphology from the projected images. The analysis is conducted using ImageJ 1.47 (Image J 2013).

The diameter of primary particles, d_p, is determined from the images by measuring the surface area of circles drawn on the periphery of readily identifiable primary particles, generally located near the outer edge of aggregates. The number of primary particles per aggregate, n_p, can be estimated from the projected area of aggregates using a power-law relationship (Köylü and Faeth 1992; Köylü et al. 1995),

$$n_p = k_a \left(\frac{A_a}{A_p}\right)^{\alpha}, \quad [2]$$

where A_a is the projected area of individual aggregates, determined automatically from ImageJ, and A_p is the mean projected area of primary particles. Based on the findings of Köylü et al. (1995, 1997), $k_a = 1.15$ and $\alpha = 1.09$ have been used to calculate n_p.

By definition, n_p scales with the characteristic length of aggregates according to a power-law relationship (Köylü et al. 1995),

$$n_p = k_L \left(\frac{L}{d_p}\right)^{D_f} = k_f \left(\frac{2R_g}{d_p}\right)^{D_f}. \quad [3]$$

In Equation (3), L is the Feret length of an aggregate, R_g is its radius of gyration, D_f is the fractal dimension, k_f is the fractal prefactor, and k_L is a correlation constant. D_f represents the degree of compactness of fractal aggregates and k_f is a proportionality constant that describes how primary particles are packed in space (Sorensen and Roberts 1997; Liu and Mishchenko 2005).

In the present work, n_p is obtained from the particles in the TEM images by applying Equation (2), using A_a and A_p provided by ImageJ. L is also determined using Image J. The slope and the intercept of a least-square straight fit to $\log(n_p)$ as a function of $\log(L/d_p)$ yield D_f and k_L, respectively, based on Equation (3). k_f is then calculated using k_L and D_f using the following approximation (Köylü et al. 1995),

$$\frac{k_f}{k_L} = \left(\frac{D_f + 2}{D_f}\right)^{\frac{D_f}{2}}, \quad [4]$$

which enables calculating the radii of gyration of aggregates using Equation (3).

The relationships between the actual, e.g., n_p, and the projected, e.g., L, R_g, and A_a, morphological properties of soot aggregates are relatively independent of fuel type and combustion configuration (Köylü and Faeth 1992; Köylü et al. 1995; Sander 1986). In the present work, the values of n_p, L, R_g, and A_a, are used only to obtain D_f and k_f, and therefore are not reported in the Results sections.

3. Results

3.1. Comparing the chemical structure of soot

Figure 1 displays a comparison between the Raman spectra of the samples emitted from the fuel-rich and fuel-lean soot generator setpoints, and aircraft turbine engines, averaged over all samples for each of these three conditions, respectively. These spectra are the result of the 5-band curve fitting procedure to the experimental results, as documented in Section 3 of the SI. The spectra have been normalized to the peak of the D band. There is an excellent agreement between the averaged spectra of the fuel-lean and the engine samples. However, the spectrum of the fuel-rich samples shows a shoulder on the D band, over the 1150–1280 cm^{-1} frequency range, which is not observed in the spectra of the lean-flame and the engine samples. In addition, the rich-flame spectrum depicts a more-intense peak between 1600 and 1620 cm^{-1}, compared to the lean-flame and the engine spectra.

To separate the contribution of each band to the cumulative fit and to find the source of the differences depicted in Figure 1, Table 5 shows the ratios of the average intensities (I) of the individual bands to the intensity of the whole Raman spectrum for the rich-flame, lean-flame, and engine samples. These intensities are characterized using the areas under the individual bands of the Raman spectra, and the ratios represent the fractional contribution of each band to the total. The average intensity of the D_4 band for the rich-flame samples is 150%

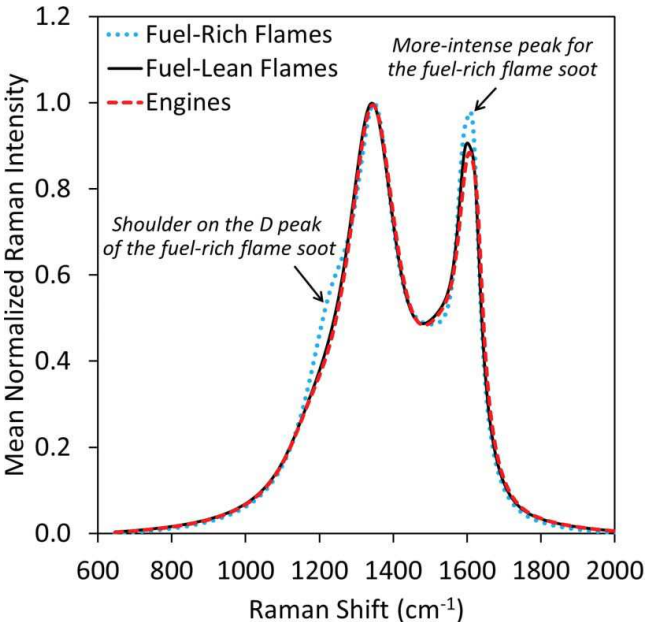

Figure 1. A comparison between the normalized averaged Raman spectra of the soot emitted from the fuel-rich flames, fuel-lean flames, and aircraft turbine engines.

Table 5. The ratios of the intensities of the individual bands to the intensity of the whole Raman spectrum, I(total), and the ratios of the intensities of the defect bands to the G band. Intensities are quantified by the areas under the bands. The curve-fitting approach that allows the centers, FWHMs, and intensities of the bands to vary has been used.

	Fuel-rich flames	Fuel-lean flames	Engines
$I(D_4)/I$(total)	0.25	0.10	0.09
$I(D_1)/I$(total)	0.43	0.63	0.64
$I(D_3)/I$(total)	0.13	0.12	0.12
I(G)/I(total)	0.08	0.09	0.09
$I(D_2)/I$(total)	0.11	0.06	0.06
$I(D_4)/I$(G)	3.38	1.20	1.10
$I(D_1)/I$(G)	5.84	7.30	7.93
$I(D_3)/I$(G)	1.71	1.43	1.51
$I(D_2)/I$(G)	1.54	0.74	0.77

and 178% greater than that for the lean-flame and engine samples, respectively. Therefore, the shoulder observed in Figure 2 on the D band is caused by a significantly stronger D_4 band in the Raman spectrum of the rich-flame samples, combined with a relatively weaker D_1 band. The analysis also shows that in the rich-flame Raman spectrum the intensity of the D_2 band is 83% greater and the intensity of the G band is 11% lower compared to those intensities for the lean-flame and engine Raman spectra. This indicates that the more-intense peak of the G band for the rich-flame spectrum, demonstrated in Figure 1, is primarily caused by a more-substantial contribution of the D_2 band.

To confirm that the differences observed in Figure 1 are not artifacts produced by curve fitting, Figure S5a, in the SI, shows a comparison between the measured Raman spectra averaged for the three groups of samples. Similar to Figure 1, a shoulder on the D band and a stronger peak between 1600 and 1620 cm^{-1} are observed in this figure for the samples emitted under fuel-rich conditions, as compared to the samples under fuel-lean conditions and from the engine. As an additional step to verify the differences shown in Figure 1, the curve-fitting procedure has been conducted individually for each of the soot-generator and engine setpoints by fixing the centers and FWHMs of the five bands to the values shown in Table 4, such that the fitting parameters are only the amplitudes of the five bands. The results, presented in Figure S5b, also demonstrate a distinct shoulder on the D band and a more-intense peak between 1600 and 1620 cm^{-1} for the fuel-rich setpoints of the soot generator. Figure S7 shows the uncertainties associated with curve fitting for some of the averaged Raman spectral parameters shown in Table 5. These uncertainties are calculated by the OriginPro 9.1.0 (2013). Based on Figure S7, the difference between the intensity ratios $I(D_1)/I$(total), $I(D_2)/I$(total), and $I(D_4)/I$(total) for the three groups of soot samples is larger than the

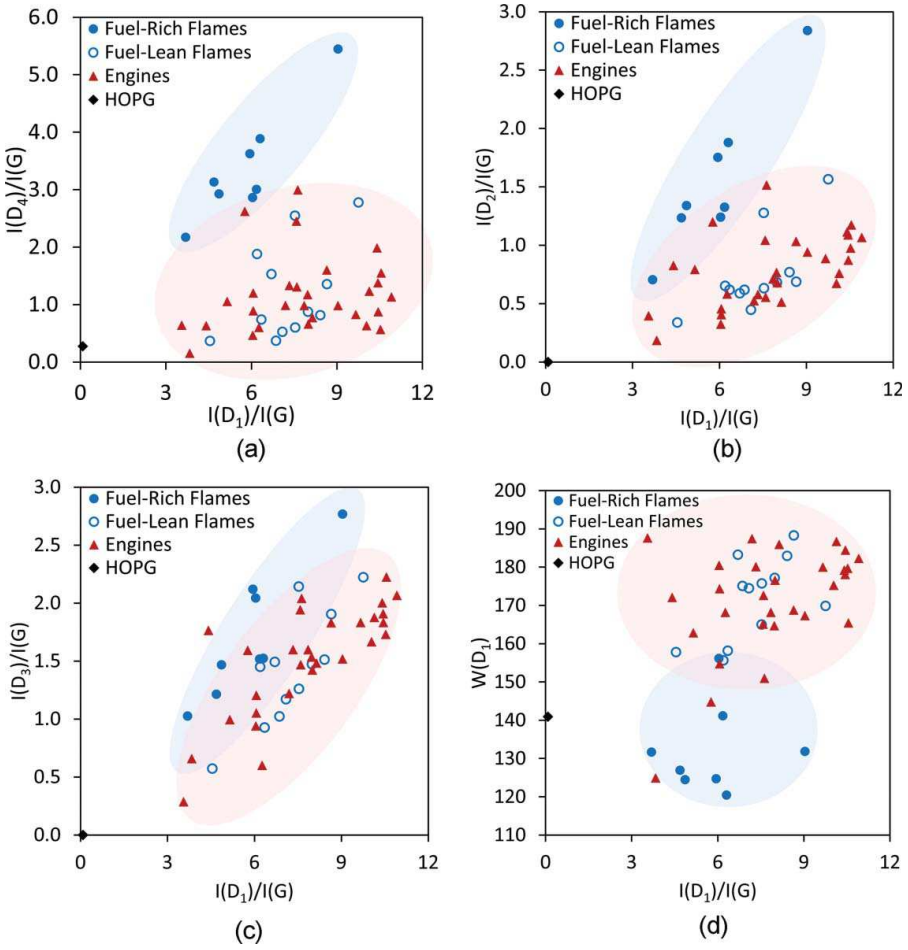

Figure 2. Comparisons between different Raman spectral parameters of soot particles emitted from the fuel-rich flames, fuel-lean flames, the aircraft turbine engines, and HOPG.

uncertainties of these parameters, thereby these differences are statistically significant and can be used to compare the properties of the samples.

Based on the information presented in Table 3 on the physical nature of the bands that construct the Raman spectrum of carbonaceous material, the ratio of D_2-band intensity to G-band intensity, i.e., $I(D_2)/I(G)$, can act as a measure for the surface area-to-volume ratio of the graphitic crystallites. On the other hand, the ratio of the D_1-band to G-band intensities, i.e., $I(D_1)/I(G)$, is correlated with the edge-to-volume ratio of the graphite crystallites. In this work, $I(D_2)/I(G)$ is 104% greater and $I(D_1)/I(G)$ is 23% lower for the rich-flame soot compared to the lean-flame- and engine-emitted soot (Table 5). Therefore, the graphitic crystallites in the rich-flame soot samples have a considerably larger surface area-to-volume ratio and a slightly lower edge-to-volume ratio than the crystallites in the other two samples. This indicates that the graphitic crystallites in the rich-flame soot samples are thinner than those in the lean-flames and the engine samples.

If the D_4 band originates from carbon atoms with sp^3 and mixed sp^2-sp^3 hybridization states (Table 3), a lower $I(D_4)/I(G)$ indicates a higher level of graphitization with more sp^2-hybridized carbon atoms. As a result, the lean-flame and the engine samples, with an $I(D_4)/I(G)$ of about 1.15, have a higher level of structural order compared to the rich-flame samples, with an $I(D_4)/I(G)$ of 3.38. More carbon atoms with sp^2-sp^3 hybridization states in the rich-flame samples may also show the presence of a larger number of bent graphitic crystallites in the rich-flame soot and larger planar graphitic structures in the soot emitted from the lean-flame setpoints and the engines (Jäger et al. 1999). On the other hand, if the source of the D_4 band is the single carbon-carbon bonds in polyacetylene-like structures, a higher $I(D_4)/I(G)$ in the rich-flame samples suggests a higher concentration of polyacetylene compounds in soot (Shirakawa et al. 1973; Harada et al. 1980; Fitchen 1982; Ishida et al. 1986; Lopez-Rios et al. 1996).

The origins of the D_3 band are known to be amorphous-carbon and ionic impurities (Table 3). Therefore, the contribution of the D_3 band to the total Raman signal can quantify the amount of these compounds in the samples. Figure 1 and Table 5 show that the sample-to-

sample variations in $I(D_3)$ are small, hence the samples include comparable levels of non-graphitic impurities.

To enable a better comparison between the properties of soot emitted from the soot generators and the engines, the Raman spectral parameters are directly compared in Figures 2a–d. As the ratios of the intensities of the defect bands to the G band of the Raman spectrum show the greatest sensitivity, and the D_1 band has the largest fraction of the intensity, $I(D_1)/I(G)$ was selected as the abscissa for all of these comparisons. The results for each group of samples form clusters that occupy different regions in the plots. The amount of overlap between these clusters can indicate the similarity or the distinction of the chemical structure of the samples. Figure 2a compares the soot samples based on $I(D_4)/I(G)$. The rich-flame data points form a cluster that has little overlap with the engine cluster. On the other hand, there is an excellent match between the lean-flame and the engine samples. A similar behavior is observed in Figure 2b, which compares the samples based on $I(D_2)/I(G)$. Figure 2b shows that the rich-flame and the engine data points fall into two distinct clusters; however, the lean-flame and engine data points agree well. Figure 2c shows that the ratio $I(D_3)/I(G)$ does not sufficiently discriminate between the soot samples, because the intensities of the D_3 and D_1 bands are comparable for all the samples. The Raman spectral parameters of highly ordered pyrolytic graphite (HOPG), which consists of highly uniform sp^2-bonded carbon atoms in planar graphite sheets, are also added in Figure 2 for reference. HOPG results demonstrate that a sample that is known to have a predominantly crystalline graphitic structure does not have a significant proportion of defects when the Raman spectra are analyzed.

The FWHMs of the D_1 and G bands, i.e., $W(D_1)$ and W(G), have been used extensively in the literature to compare the graphitic structure of carbonaceous material (Wang et al. 1990; Dippel et al. 1999; Sadezky et al. 2005; Knauer et al. 2009; Soewono and Rogak 2011). Higher D_1 and G band FWHMs show higher levels of chemical heterogeneity and a lower degree of structural order (Knauer et al. 2009). Figure 2d depicts a plot of $W(D_1)$, dividing the data points into two distinct clusters: the rich-flame cluster with a lower $W(D_1)$, i.e., a less heterogenous structure, and the engine cluster with higher $W(D_1)$ values, i.e., a higher level of heterogeneity. Figure 2d also shows that the lean-flame setpoints produce soot with a similar graphitic structure as the engine-emitted soot. Nevertheless, Figure S8, which compares the samples based on the FWHM of the G band, does not separate the data points into distinct groups, thus indicating that the levels of chemical heterogeneity are complex and beyond the scope of this analysis.

The authors have not observed any relationship between the Raman spectral properties of engine-emitted soot and the operating speed and thrust of the engines. A similar behavior has been reported by Parent et al. (2016), who conducted a set of complementary tests, including Raman spectroscopy, to obtain information about the physical and chemical structure of soot emitted from a recent aircraft turbine engine operating under various thrust levels. The results of that study have shown that the properties of soot do not vary significantly with changing the engine operating regime.

Figure S9, in the SI, compares the Raman spectral parameters of the individual soot generator setpoints for both rich-flame and lean-flame conditions. The parameters of the duplicated setpoints are included in Figure S9 to demonstrate the repeatability of the measurements. The parameters for setpoints FR3, FR4, and FR5, which have their fuel streams diluted with 200–285 mL/min of nitrogen, are within the same range as the fuel-rich setpoints with no fuel dilution.

Carpentier et al. (2012) have proposed the presence of a sixth band, D_1' centered at 1269 cm^{-1}, in the Raman spectrum of carbonaceous particles. This band originates from the merging of the subbands characteristic of the individual polyaromatic subunits. Because the center frequency of the D_1' band is within the frequency range of the shoulder observed on the D band for the fuel-rich flame samples, a six-band curve fit has also been conducted (shown in Figure S4). A comparison between the Raman spectral parameters calculated based on the six-band curve fit, presented in Figure S6, shows that this approach does not distinguish the differences between the Raman signatures of the samples well. Therefore, the discussion and conclusions in the present work are based on the well-established five-band curve fitting approach.

3.2. Comparing the size and morphology of soot

Figure 3 depicts TEM images of typical soot particles emitted from the MiniCAST soot generator and turboshaft engine 1, at a TEM magnification level of 45,000 times. These images show a clear distinction between the physical structures of particles sampled from fuel-rich flames, fuel-lean flames, and an engine. TEM images captured using a magnification of 4500 times and the TEM images in Figure 3 shown in a larger size are depicted in Figures S10–S29 in the SI.

The TEM images of the particles from the fuel-rich flames are shown in Figures 3a–c. The particles emitted at FR1 and FR2 setpoints (Figures 3a and b) have an amorphous appearance, with less-distinctive boundaries between primary particles, suggesting that these

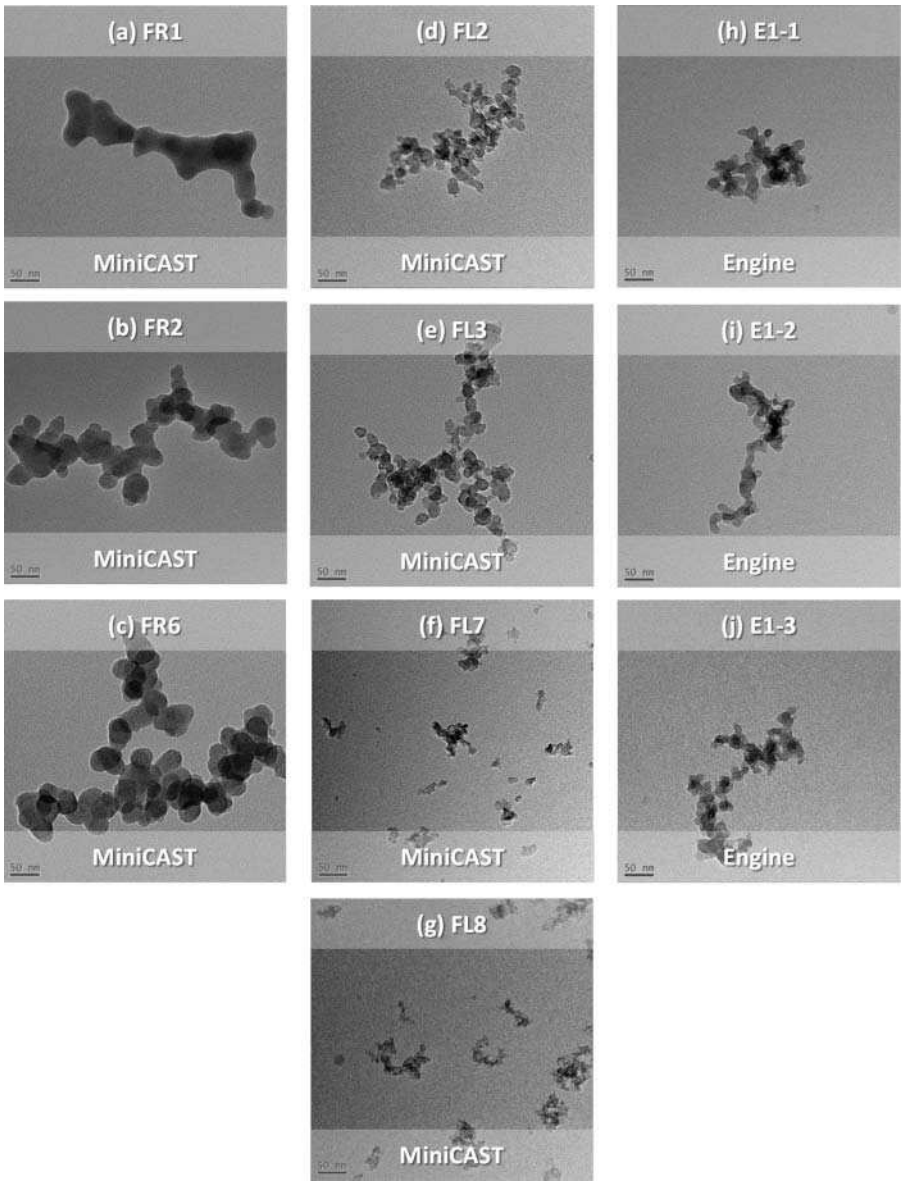

Figure 3. Typical TEM images of soot produced by the fuel-rich MiniCAST flames (a–c), fuel-lean MiniCAST flames (d–g), and turboshaft engine 1 (h–j) at a magnification of 45,000 times. These images in larger size and images captured with a magnification of 4500 times are provided in the SI.

aggregates are coated with a considerable amount of semivolatile material. On the other hand, the particles emitted at the FR6 setpoint (Figure 3c) have a more-graphitized appearance with no evidence of significant semivolatile coatings.

The particles emitted at the lean-flame setpoints (Figures 3d–g) appear to have smaller primary particles compared to the rich-flame setpoints, in particular at FL7 and FL8 setpoints. The particles emitted at FL7 and FL8 setpoints have an amorphous appearance and are significantly smaller than the particles emitted at the fuel-rich and the FL2 and FL3 setpoints. These differences are most likely because the particles at FL7 and FL8 setpoints are heavily oxidized.

The images of particles emitted from turboshaft engine 1 (Figures 3h–j) show particles with small primary particles, similar to those emitted at the lean-flame MiniCAST setpoints, and no evidence of significant semivolatile coatings. The size of the aggregates emitted from the engine is also fairly small, particularly at the E1-1 setpoint.

Table 6 presents the results of TEM image analysis for the size and morphological parameters of particles shown in Figure 3, including the diameter of primary particles (d_p), and the diameter (D_a), fractal dimension (D_f), and fractal prefactor (k_f) of soot aggregates. The diameter of soot aggregates is characterized by the projected equivalent-area diameter, which is defined as the

Table 6. The results of TEM image analysis for particle size and morphology, st. dev. = standard deviation.

	Primary particles			Soot aggregates				
Setpoint	d_p mean (nm)	d_p st. dev. (nm)	Number of samples	D_a mean (nm)	D_a st. dev. (nm)	D_f	k_f	Number of samples
FR1	38.9	9.4	98	81.9	43.3	1.6	1.9	1577
FR2	40.5	8.8	111	103.1	71.4	1.8	1.7	1454
FR6	31.7	6.1	403	111.8	68.4	1.8	1.7	1248
FL2	18.5	3.2	31	64.3	49.3	1.8	0.7	7403
FL3	22.5	4.3	199	63.3	43.9	1.7	0.9	1701
FL7	15.0	3.7	58	24.2	10.0	1.6	1.5	24,672
FL8	9.4	1.6	23	27.0	16.7	1.8	0.3	27,816
E1-1	17.2	3.5	61	33.5	25.5	1.6	1.5	1543
E1-2	20.8	4.9	40	45.7	28.3	1.7	1.2	3509
E1-3	21.5	5.3	49	44.2	28.5	1.8	1.1	1738

diameter of a circle with the same area as the projected area of the aggregate. The standard deviations for the d_p are 17 to 25% of the mean values, representative of a nearly monodisperse size distribution. Contrary to primary particles, soot aggregates are polydisperse and have highly uneven sizes, with standard deviations for the distributions of the aggregate properties between 41 and 77%.

The diameters of primary particles, averaged over the rich-flame, lean-flame, and engine setpoints, are 34.4 nm, 20.6 nm, and 19.6 nm, respectively. The mean d_p values for the rich-flame setpoint are about 70% larger than d_p for the engine setpoints; however, there is a good agreement between d_p for lean-flame setpoints and the engine (5% difference). A similar behavior is observed for the diameters of soot aggregates. D_a averaged over the rich-flame setpoints is 97.8 nm, which is 130% larger than averaged D_a for the engine setpoints (42.5 nm). On the other hand, D_a is 34.9 for the lean-flame setpoints, which is similar to (17% smaller than) D_a of engine-emitted particles.

Figures 4a and b compare the physical properties of soot particles emitted from the soot generators and turboshaft engine 1 based on their size and morphology, respectively. Figure 4a shows that d_p and D_a of soot particles emitted by the rich-flame setpoints are larger than 30 nm and 70 nm, respectively. However, d_p and D_a of the soot emitted from turboshaft engine 1 are below 25 nm and 50 nm, respectively. Therefore, these data points form two very distinct clusters in Figure 4a. On the other hand, d_p and D_a for soot emitted from the lean-flame setpoints are close to the d_p and D_a of engine-emitted soot.

A similar behavior is observed in Figure 4b, which compares particles based on their morphological properties, D_f and k_f. The average fractal dimension for all aggregates is 1.72 with a standard deviation of 5%. Combustion-generated particulates are formed by a diffusion-limited cluster−cluster aggregation mechanism (Sander 1986). Therefore, the fractal dimension of soot aggregates is universal and nearly independent of combustion condition. However, the variations in k_f are significant, as depicted by a standard deviation of 41% for all aggregates around the mean value of 1.23. The particles emitted from the MiniCAST at fuel-rich conditions have a k_f between 1.6 and 2.0, while the k_f of particles emitted

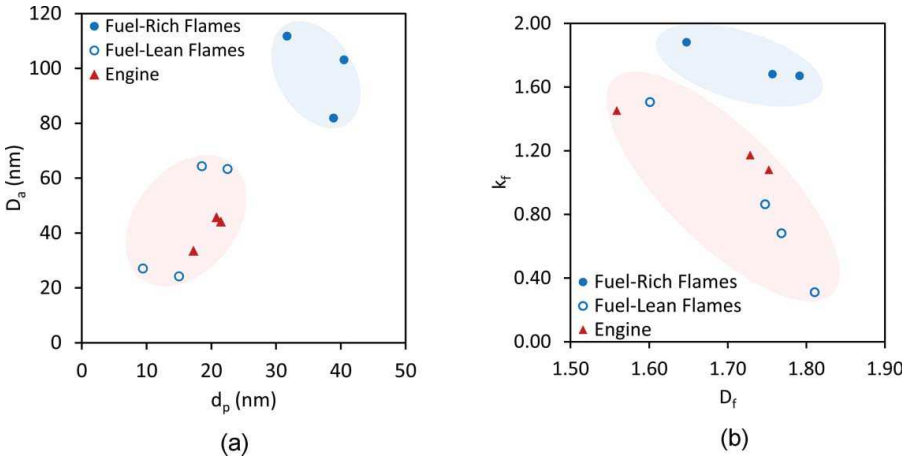

Figure 4. A comparison between the size and morphological parameters of soot particles emitted from the fuel-rich MiniCAST flames, fuel-lean MiniCAST flames, and turboshaft engine 1.

from the fuel-lean MiniCAST setpoints and the engine varies between 0.3 and 1.6. The higher k_f of particles emitted from fuel-rich flames shows that these aggregates have a more compact structure (Liu and Mishchenko 2005). The difference in the k_f values causes two separate clusters to appear in Figure 4b.

Plotting the data points based on Raman spectral parameters and d_p, shown in Figure S30, also results in distinctly different clusters for the fuel-rich flame and the engine data points. However, these properties are very close for the fuel-lean flames and the engine.

To compare the radiative properties of flame- and engine-emitted soot, Maricq (2014) measured the BC content of particles generated by a MiniCAST 5201 C, operating with a constant fuel flow rate of 60 mL/min and five different fuel N_2 dilution levels from 0 to 300 mL/min, and those emitted from four vehicles operating under different driving conditions. The results have shown that this MiniCAST produces soot with similar BC content as vehicle-emitted soot only when the fuel dilution levels were below 100 mL/min. For higher fuel dilution levels, Maricq (2014) found that the emitted soot is not sufficiently carbonized because of a higher fuel-stream velocity and a shorter residence time of particles, thereby it cannot act as a surrogate for engine-emitted soot. To match the chemical structure, size, and morphology of soot emitted from gas turbine engines, the present work shows that the ratio of air to fuel flow rates in the MiniCAST should also be sufficient to adequately oxidize the emitted soot.

In another study, Mamakos et al. (2013) studied the effective densities, elemental-carbon (EC) and organic-carbon (OC) contents, light absorption characteristics, and primary-particle diameters of soot generated by a MiniCAST 5200, operating under seven different conditions. Similar to the present work, the authors have found that increasing the fuel-to-air ratio results in the emission of premature soot particles with high semivolatile content. On the other hand, Mamakos et al. (2013) found that lower fuel and higher air flow rates cause the formation of high-EC soot with high light-absorption capability.

Moore et al. (2014) have also conducted a thorough characterization of the properties of soot, generated by a MiniCAST model 4202, to guide the selection of optimum setpoints. The properties of MiniCAST soot have also been compared to those reported in the literature for soot emitted from diesel and gas-turbine engines. The MiniCAST operated under three different regimes: (1) fuel-rich flame and high-OC soot, (2) fuel-lean flame and low-OC soot, and (3) fuel-lean flame and high-OC soot. From Table 1 of Moore et al. (2014), it can be concluded that high-OC soot generated under fuel-lean conditions represent the properties of aircraft-emitted soot better that the other two operating regimes. To compare the results of the present work with those of Moore et al., the EC-to-TC ratios of soot samples studied herein are shown in Tables S3 and S4 in the SI. The mean EC/TC for engine-emitted samples is 0.59, which can be reproduced by highly fuel-rich (e.g., FR1) and highly fuel-lean (e.g., FL7 and FL8) setpoints of the MiniCAST. On the other hand, the Raman spectroscopy and TEM studies, presented earlier in this section, have shown that only the lean-flame samples represent the chemical structure and morphology of engine-emitted soot. Therefore, the findings of this study are in agreement with those of Moore et al. (2014), with the additional basis in terms of chemical structure and morphology.

4. Conclusions

To compare the chemical structure, size, and morphology of soot particles emitted from engines to those produced by laboratory soot generators, Raman spectroscopy, and transmission electron microscopy studies have been conducted for the soot samples. The results of this study can be used to identify soot generator setpoints that produce particles with similar chemical and physical properties to the soot emitted from engines. As the optical properties of soot are dictated by its chemical structure, size, and morphology, and many of the instruments that measure mass concentrations of solid particulate matter in the exhaust emissions from engines rely on the optical properties of soot, finding these soot generator setpoints can be applied to enhance the reliability of instrument calibrations. While this study was applied to aircraft gas turbine engine emissions, the principles in identifying the chemical structure, size, and morphology of soot particles may be applicable to finding soot generator operating conditions that produce particles with similar characteristics from other engines, such as Diesel engines and gasoline direct injection engines. The important findings of this study are summarized below:

1. The Raman spectral properties, and thereby the chemical structure, of the soot generated by the fuel-rich soot-generator flames, with globally near-stoichiometric and fuel-rich combustion, are considerably different from the spectral properties and chemical structure of the soot emitted from aircraft turbine engines. The differences are mainly caused by (1) thinner graphitic crystallites of the soot emitted from the fuel-rich flames, (2) a larger number of sp^2-hybridized carbon atoms in the lean-flame and the engine samples, and (3) a larger

number of bent graphitic crystallites or polyacetylene compounds in the rich-flame samples.

2. The size of primary soot particles and aggregates emitted from the fuel-rich soot-generator flames is considerably larger than the size of particles emitted from a turboshaft engine. While the reasons for these differences are not well understood, it was noted that there was the appearance of condensed organic material on soot particles emitted from the fuel-rich flames and a more intense oxidation of the soot emitted from the fuel-lean flames and the engine.
3. Good agreement has been found between the chemical structure, size, and morphology of the soot emitted from the soot generators operating under fuel-lean conditions and the properties of soot emitted from the aircraft turbine engines. Comparable combustion conditions, in particular similar global equivalence ratios, contribute to the concurrence of the soot properties. It should be noted that soot formation is not suppressed in the oxygen-abundant fuel-lean diffusion flames used in the present work, but occurs under a combustion condition that is different from that in the fuel-rich flames.
4. The fractal dimensions of soot particles emitted from the soot generators and the turbine engines, at all setpoints, are within the same range. However, the fractal prefactor of particles emitted from the fuel-rich flames are higher than that for particles emitted from the fuel-lean flames and the turboshaft engine, suggesting that the particles emitted from the fuel-rich flames have a more compact arrangement.
5. Overall, the key parameters that were found to distinguish soot particle emissions produced by aircraft gas turbine engines from those produced by rich-flame soot generator conditions were: for chemical structure, the $I(D_4)/I(G)$ ratio found from a five-band fit to the Raman spectrum, and to a lesser extent the $I(D_2)/I(G)$ ratio; for size and morphology, the diameters of the primary particles, the diameters of the aggregates, and the fractal prefactor.

These conclusions are based on measurements conducted for three aviation engines and two soot generators operating under a limited number of conditions. Therefore, more data for other types of engines and soot generators is required before one can generalize these conclusions. Although this work has identified soot generator setpoints that emit soot with similar chemical structure, size, and morphology as the soot emitted from aircraft turbine engines, it has not demonstrated the advantage of calibrating optical instruments for measuring mass concentration of solid particulate matter with these recommended setpoints. The validation of these setpoints is a topic for future work.

Acknowledgments

Access to the turboshaft engines and the fuel were provided by Rolls-Royce UK. The authors thank all the personnel involved during the Mass Assessment of nvPM Technology Readiness for Aviation (MANTRA) measurement campaigns.

Funding

Financial support for this work was provided by Transport Canada, through the Development and Applications of Particulate Matter Measurements for Gas Turbine Engines project under the Clean Transportation Program. Emissions sampling on the turbofan engine was supported by the Swiss Federal Office of Civil Aviation.

References

Adachi, K., Chung, S. H., Friedrich, H., and Buseck, P. R. (2007). Fractal Parameters of Individual Soot Particles Determined using Electron Tomography: Implications for Optical Properties. *J. Geophys. Res. Atmos.*, 112(D14):1–10.

Bacsa, W. S., Lannin, J. S., Pappas, D. L., and Cuomo, J. J. (1993). Raman Scattering of Laser-Deposited Amorphous Carbon. *Phys. Rev. B*, 47(16):10931–10934.

Baumgardner, D., Popovicheva, O., Allan, J., Bernardoni, V., Cao, J., Cavalli, F., Cozic, J., Diapouli, E., Eleftheriadis, K., Genberg, P. J., and Gonzalez, C. (2012). Soot Reference Materials for Instrument Calibration and Intercomparisons: A Workshop Summary with Recommendations. *Atmos. Meas. Tech.*, 5:1869–1887.

Bond, T. C., Doherty, S. J., Fahey, D. W., Forster, P. M., Berntsen, T., DeAngelo, B. J., Flanner, M. G., Ghan, S., Kärcher, B., Koch, D., and Kinne, S. (2013). Bounding the Role of Black Carbon in the Climate System: A Scientific Assessment. *J. Geophys. Res. Atmos.*, 118(11):5380–5552.

Boyle, K. (1996). Evaluating Particulate Emissions from Jet Engines: Analysis of Chemical and Physical Characteristics and Potential Impacts on Coastal Environments and Human Health. *Trans. Res. Rec. J. Trans. Res. Board*, 1517:1–9. DOI: 10.3141/1517-01.

Carpentier, Y., Féraud, G., Dartois, E., Brunetto, R., Charon, E., Cao, A. T., d'Hendecourt, L., Bréchignac, Ph., Rouzaud, J.-N., and Pino, T. (2012). Nanostructuration of Carbonaceous Dust as Seen Through the Positions of the 6.2 and 7.7 μm AIBs. *Astron. Astrophys.*, 548(A40):1–14.

Coderre, A. R., Thomson, K. A., Snelling, D. R., and Johnson, M. R. (2011). Spectrally Resolved Light Absorption Properties of Cooled Soot from a Methane Flame. *Appl. Phys. B*, 104(1):175–188.

Colbeck, I., Atkinson, B., and Johar, Y. (1997). The Morphology and Optical Properties of Soot Produced by Different Fuels. *J. Aerosol Sci.*, 28(5):715–723.

Cuesta, A., Dhamelincourt, P., Laureyns, J., Martinez-Alonso, A., and Tascón, J. D. (1994). Raman Microprobe Studies on Carbon Materials. *Carbon*, 32(8):1523–1532.

Denman, K. L., and Brasseur, G. (2007). Couplings Between Changes in the Climate System and Biogeochemistry, in *Contribution of Working Group I to the fourth Assessment Report of the Intergovernmental Panel on Climate Change*, S. Solomon, D. Qin, M. Manning, Z. Chen, M. Marquis, K. B. Averyt, M. Tignor, H. L. Miller, eds., Cambridge University Press, Cambridge, pp. 499–587.

Dippel, B., Jander, H., and Heintzenberg, J. (1999). NIR FT Raman Spectroscopic Study of Flame Soot. *Phys. Chem. Chem. Phys.*, 1(20):4707–4712.

Dobbins, R. A., and Megaridis, C. M. (1987). Morphology of Flame-Generated Soot as Determined by Thermophoretic Sampling. *Langmuir*, 3(2):254–259.

Donaldson, K., Stone, V., Seaton, A., and MacNee, W. (2001). Ambient Particle Inhalation and the Cardiovascular System: Potential Mechanisms. *Environ. Health Perspect.*, 109 (Suppl. 4):523–527.

Dresselhaus, M. S., and Dresselhaus, G. (1982). Light Scattering in Graphite Intercalation Compounds, in *Light Scattering in Solids III*, M. Cardona and G. Güntherodt, eds., Springer, Berlin. pp. 3–57.

Faeth, G. M., and Köylü, Ü. Ö. (1995). Soot Morphology and Optical Properties in Nonpremixed Turbulent Flame Environments. *Combust. Sci. Technol.*, 108(4–6):207–229.

Fitchen, D. B. (1982). Resonance Raman Results in Polyacetylene. *Mol. Cryst. Liq. Cryst.*, 83(1):95–108.

Forster, P., and Ramaswamy, V. (2007). Changes in Atmospheric Constituents and in Radiative Forcing, in *Contribution of Working Group I to the fourth assessment report of the Intergovernmental Panel on Climate Change*, S. Solomon, D. Qin, M. Manning, Z. Chen, M. Marquis, K. B. Averyt, M. Tignor, H. L. Miller, eds., Cambridge University Press, Cambridge. pp. 129–234.

Ghazi, R., Tjong, H., Soewono, A., Rogak, S. N., and Olfert, J. S. (2013). Mass, Mobility, Volatility, and Morphology of Soot Particles Generated by a McKenna and Inverted Burner. *Aerosol Sci. Technol.*, 47(4):395–405.

Giechaskiel, B., Cresnoverh, M., Jörgl, H., and Bergmann, A. (2010). Calibration and Accuracy of a Particle Number Measurement System. *Meas. Sci. Technol.*, 21(4):045102–045114.

Gysel, M., Laborde, M., Mensah, A. A., Corbin, J. C., Keller, A., Kim, J., Petzold, A., and Sierau, B. (2012). Technical Note: The Single Particle Soot Photometer Fails to Reliably Detect PALAS Soot Nanoparticles. *Atmos. Meas. Tech.*, 5(12):3099–3107.

Harada, I., Furukawa, Y., Tasumi, M., Shirakawa, H., and Ikeda, S. (1980). Spectroscopic Studies on Doped Polyacetylene and β-Carotene. *J. Chem. Phys.*, 73(10):4746–4757.

Hudda, N., Gould, T., Hartin, K., Larson, T. V., and Fruin, S. A. (2014). Emissions from an International Airport Increase Particle Number Concentrations 4–fold at 10 km Downwind. *Environ. Sci. Technol.*, 48(12):6628–6635.

Image, J. 1.47, National Institute of Health, USA. Available at: https://imagej.nih.gov/ij.

Ishida, H., Fukuda, H., Katagiri, G., and Ishitani, A. (1986). An Application of Surface-Enhanced Raman Scattering to the Surface Characterization of Carbon Materials. *Appl. Spectr.*, 40(3):322–330.

Jäger, C., Henning, T., Schlögl, R., and Spillecke, O. (1999). Spectral Properties of Carbon Black. *J. Non-Cryst. Solids*, 258(1):161–179.

Jawhari, T., Roid, A., and Casado, J. (1995). Raman Spectroscopic Characterization of Some Commercially Available Carbon Black Materials. *Carbon*, 33(11): 1561–1565.

Knauer, M., Carrara, M., Rothe, D., Niessner, R., and Ivleva, N. P. (2009). Changes in Structure and Reactivity of Soot During Oxidation and Gasification by Oxygen, Studied by Micro-Raman Spectroscopy and Temperature Programmed Oxidation. *Aerosol Sci. Technol.*, 43(1):1–8.

Köylü, Ü. Ö., and Faeth, G. M. (1992). Structure of Overfire Soot in Buoyant Turbulent Diffusion Flames at Long Residence Times. *Combust. Flame*, 89(2):140–156.

Köylü, Ü. Ö., McEnally, C. S., Rosner, D. E., and Pfefferle, L. D. (1997). Simultaneous Measurements of Soot Volume Fraction and Particle Size/Microstructure in Flames using a Thermophoretic Sampling Technique. *Combust. Flame*, 110 (4):494–507.

Köylü, Ü. Ö., Xing, Y., and Rosner, D. E. (1995). Fractal Morphology Analysis of Combustion-Generated Aggregates using Angular Light Scattering and Electron Microscope Images. *Langmuir*, 11(12):4848–4854.

Liousse, C., Cachier, H., and Jennings, S. G. (1993). Optical and Thermal Measurements of Black Carbon Aerosol Content in Different Environments: Variation of the Specific Attenuation Cross-Section, Sigma (σ). *Atmos. Environ. Part A. Gen. Top.*, 27(8):1203–1211.

Liu, L., and Mishchenko, M. I. (2005). Effects of Aggregation on Scattering and Radiative Properties of Soot Aerosols. *J. Geophys. Res.: Atmos.*, 110(D11211):1–10.

Lopez-Rios, T., Sandre, E., Leclercq, S., and Sauvain, E. (1996). Polyacetylene in Diamond Films Evidenced by Surface Enhanced Raman Scattering. *Phys. Rev. Lett.*, 76(26):4935–4938.

Mamakos, A., Khalek, I., Giannelli, R., and Spears, M. (2013). Characterization of Combustion Aerosol Produced by a Mini-CAST and Treated in a Catalytic Stripper. *Aerosol Sci. Technol.*, 47(8):927–936.

Maricq, M. M. (2014). Examining the Relationship between Black Carbon and Soot in Flames and Engine Exhaust. *Aerosol Sci. Technol.*, 48(6):620–629.

MDPH – Massachusetts Department of Public Health. (2014). Logan Airport Health Study. Available at: http://www.mass.gov/eohhs/gov/departments/dph/programs/environmental-health/investigations/logan-airport-health-study.html.

Mertes, S., Dippel, B., and Schwarzenböck, A. (2004). Quantification of Graphitic Carbon in Atmospheric Aerosol Particles by Raman Spectroscopy and First Application for the Determination of Mass Absorption Efficiencies. *J. Aerosol Sci.*, 35(3):347–361.

Miller, A., Frey, G., King, G., and Sunderman, C. (2010). A Handheld Electrostatic Precipitator for Sampling Airborne Particles and Nanoparticles. *Aerosol Sci. Technol.*, 44 (6):417–427.

Moore, R. H., Ziemba, L. D., Dutcher, D., Beyersdorf, A. J., Chan, K., Crumeyrolle, S., Raymond, T. M., Thornhill, K. L., Winstead, E. L., and Anderson, B. E. (2014). Mapping the Operation of the Miniature Combustion Aerosol Standard (Mini-CAST) Soot Generator. *Aerosol Sci. Technol.*, 48(5):467–479.

OriginPro 9.1.0. (2013). OriginPro 9.1.0. Version 9.1.0 (64–bit) Sr2, OriginLab Corporation, USA. Available at: http://www.originlab.com.

Parent, P., Laffon, C., Marhaba, I., Ferry, D., Regier, T. Z., Ortega, I. K., Chazallon, B., Carpentier, Y., and Focsa, C. (2016). Nanoscale Characterization of Aircraft Soot: A High-Resolution Transmission Electron Microscopy, Raman Spectroscopy, X-ray Photoelectron and Near-Edge X-ray Absorption Spectroscopy Study. *Carbon*, 101:86–100.

Pimenta, M. A., Dresselhaus, G., Dresselhaus, M. S., Cancado, L. G., Jorio, A., and Saito, R. (2007). Studying Disorder in Graphite-Based Systems by Raman Spectroscopy. *Physical Chemistry Chemical Physics*, 9(11):1276–1290.

Pope 3rd, C. A. (2000). Epidemiology of Fine Particulate Air Pollution and Human Health: Biologic Mechanisms and Who's at Risk? *Environ. Health Perspect.*, 108(Suppl 4): 713–723.

Raj, A., Sander, M., Janardhanan, V., and Kraft, M. (2010). A Study on the Coagulation of Polycyclic Aromatic Hydrocarbon Clusters to Determine their Collision Efficiency. *Combust. Flame*, 157(3):523–534.

Rosen, H., Hansen, A. D. A., Gundel, L., and Novakov, T. (1978). Identification of the Optically Absorbing Component in Urban Aerosols. *Appl. Opt.*, 17(24):3859–3861.

Sadezky, A., Muckenhuber, H., Grothe, H., Niessner, R., and Pöschl, U. (2005). Raman Microspectroscopy of Soot and Related Carbonaceous Materials: Spectral Analysis and Structural Information. *Carbon*, 43(8):1731–1742.

SAE AIR6241. (2013). Procedure for the Continuous Sampling and Measurement of Non-Volatile Particle Emissions from Aircraft Turbine Engines. *SAE International*. Available at: http://standards.sae.org/air6241.

Saffaripour, M., Zabeti, P., Kholghy, M., and Thomson, M. J. (2011). An Experimental Comparison of the Sooting Behavior of Synthetic Jet Fuels. *Energy Fuels*, 25(12):5584–5593.

Sander, L. M. (1986). Fractal Growth Processes. *Nature*, 322 (6082):789–793.

Shaddix, C. R., Palotás, Á. B., Megaridis, C. M., Choi, M. Y., and Yang, N. Y. (2005). Soot Graphitic Order in Laminar Diffusion Flames and a Large-Scale JP-8 Pool Fire. *Int. J. Heat Mass Trans.*, 48(17):3604–3614.

Sharma, S., Brook, J. R., Cachier, H., Chow, J., Gaudenzi, A., and Lu, G. (2002). Light Absorption and Thermal Measurements of Black Carbon in Different Regions of Canada. *J. Geophys. Res. Atmos.*, 107(D24):4771–4781.

Shirakawa, H., Ito, T., and Ikeda, S. (1973). Raman Scattering and Electronic Spectra of Poly (Acetylene). *Poly. J.*, 4(4):460–462.

Slowik, J. G., Cross, E. S., Han, J. H., Davidovits, P., Onasch, T. B., Jayne, J. T., Williams, L. R., Canagaratna, M. R., Worsnop, D. R., Chakrabarty, R. K., Moosmüller, H., Arnott, W. P., Schwarz, J. P., Gao, R.-S., Fahey, D. W., Kok, G. L., and Petzold, A. (2007). An Inter-Comparison of Instruments Measuring Black Carbon Content of Soot Particles. *Aerosol Sci. Technol.*, 41(3):295–314.

Soewono, A., and Rogak, S. (2011). Morphology and Raman Spectra of Engine-Emitted Particulates. *Aerosol Sci. Technol.*, 45(10):1206–1216.

Sorensen, C. M., and Roberts, G. C. (1997). The Prefactor of Fractal Aggregates. *J. Colloid Interf. Sci.*, 186(2):447–452.

Stipe, C. B., Higgins, B. S., Lucas, D., Koshland, C. P., and Sawyer, R. F. (2005). Inverted Co-Flow Diffusion Flame for Producing Soot. *Rev. Sci. Instr.*, 76(2):023908.

Sze, S. K., Siddique, N., Sloan, J. J., and Escribano, R. (2001). Raman Spectroscopic Characterization of Carbonaceous Aerosols. *Atmos. Environ.*, 35(3):561–568.

Vander Wal, R. L. (2005). Soot Nanostructure: Definition, Quantification and Implications. *SAE Technical Paper*, No. *2005–01–0964*.

Vander Wal, R. L., and Tomasek, A. J. (2004). Soot Nanostructure: Dependence Upon Synthesis Conditions. *Combust. Flame*, 136(1):129–140.

Wang, Y., Alsmeyer, D. C., and McCreery, R. L. (1990). Raman Spectroscopy of Carbon Materials: Structural Basis of Observed Spectra. *Chem. Mater.*, 2(5):557–563.